Geochemical Perspectives Letters

Experimental evidence for light Ba isotopes favouring aqueous fluids over silicate melts

H. Guo, W.-Y. Li, X. Nan, F. Huang

Supplementary Information

The Supplementary Information includes:

- Starting Materials and Encapsulation
- High Temperature and Pressure Experiments
- Run Product Separation and Dissolution
- Barium Concentration Analyses
- Barium Isotope Analyses
- Rayleigh Fractionation Model
- Figures S-1 to S-5
- Supplementary Information References

Starting Materials and Encapsulation

The starting haplogranitic glasses were prepared from stoichiometric mixtures of analytical grade SiO_2, $Al(OH)_3$, Na_2CO_3, and K_2CO_3. The haplogranitic composition corresponds to the 2 kbar haplogranite eutectic melt composition ($Qz_{35}Ab_{40}Or_{25}$; Johannes and Holtz, 1996), and the alumina saturation index (ASI) was set to be 0.8, 1.0 and 1.2 by varying the amounts of $Al(OH)_3$, Na_2CO_3, and K_2CO_3 at a constant Na/K-ratio. The mixtures were dehydrated and decarbonated in a platinum crucible by heating from room temperature to 1100 °C at a rate of 100 °C /h and holding at 1100 °C for a further 12 h in a muffle furnace. The recovered samples were ground to fine powders in an agate mortar until they were homogenised and free of gas bubbles, then melted at 1600 °C for 2 h in a platinum crucible and quenched in distilled water. Part of these glass powders were then doped with ~1000 ppm Ba by mixing them thoroughly with $Ba(NO_3)_2$. The Ba-doped glass powders were heated at 1100 °C for 12 h to remove nitrogen

($Ba(NO_3)_2$ was decomposed to BaO and NO_2 at this temperature) and then remelted at 1600 °C in a platinum crucible for 2 h in the furnace. Aqueous fluids with the (Na, K)Cl (Na:K = 1:1 in moles) concentration of 0.5, 1 and 1.5 mol/L were prepared with deionised H_2O, analytical grade NaCl and KCl.

All experiments were conducted in Bayerisches Geoinstitut, University of Bayreuth. Silicate glass powders and the nearly similar amount of aqueous fluids (~100 mg) were loaded into Au capsules with 4.3 mm O.D. (outer diameter), 4.0 mm I.D. (inner diameter) and 2.5 mm length (Fig. S-2a). Capsules were welded and then put in an oven at 110 °C to check potential leaks, and the capsules with obvious weight changes were discarded.

High Temperature and Pressure Experiments

The capsules were then loaded into vertical rapid-quench cold-seal pressure vessels made of Inconel 713LC super alloy using water as the pressure medium, with the setup similar to that described in Matthews *et al.* (2003). Temperatures were measured with NiCr-Ni (K-type) thermocouples in an external borehole of the vessels. The uncertainties of the temperature and pressure are smaller than 5 °C and 30 bar, respectively. Oxygen fugacity was not specifically controlled in the vessels, but it should be 0.5 to 1 log unit above the Ni-NiO buffer as suggested by the reaction of water with the autoclave material (Keppler, 2010). All experiments were run at 700 to 900 °C and 200 MPa for 10 to 40 days (Table 1). The samples were quenched by dropping the external magnet to force the sample to fall into the water-cooled zone within a few seconds.

Run Product Separation and Dissolution

The capsules were recovered and weighed again to check for potential leaks during the experiments. Those without obvious weight changes were then cleaned, cooled by liquid-N_2, and then punctured with a steel needle. After the solution was withdrawn as much as possible with a micropipette, the capsules were opened and boiled in deionised water for 30 minutes. After that, they were further rinsed several times with deionized water. All solutions obtained during these operations were added together with the solution phase withdrew from the experiment. This procedure is similar to the treatment of Keppler and Wyllie (1991) in re-dissolving materials precipitated from the fluid during quenching. The capsule and recovered glass samples were dried at 130 °C in the oven for at least 2 h. Then, the Au capsule material and glass were weighed to determine the actual fluid weight after quenching by subtraction. Previous studies showed that such a method works well under relatively low-pressure experiments (<1 GPa; Borchert *et al.*, 2010; Keppler, 2017), which is suitable for the experiments conducted at 200 MPa in this study.

The solution extracted from each run product was transferred directly into a pre-cleaned screw-top Teflon beaker, and then evaporated to dryness at 100 ºC on a hot plate. The dried residue was dissolved in 2 mL concentrated HCl (all of the acids used in this study throughout the dissolution and purification processes were produced by double sub-boiling distillation). The solution was divided into two parts and processed as follows: (1) 0.1 mL of the solution was transferred into a pre-cleaned Teflon tube, and then diluted to 3 mL for Ba concentration analyses; (2) the other 1.9 mL

of the solution was evaporated to dryness, and then diluted with 3 mol/L HCl to achieve the desired Ba concentration of ~2 ppm, in preparation for column chemistry.

The melt-quenched glass in each run product was firstly ground to fine powders in an agate mortar, in order to crush fluid inclusions that were possibly trapped in the glass (Fig. S-2b). Then, the powder was transferred into a pre-cleaned Teflon tube, and rinsed with ~70 ºC ultra-pure water (18.2 MΩ.cm) for three times to remove the concomitant fluid released from fluid inclusions during crushing. Finally, the powder was dried at 105 ºC in an oven, weighed into a pre-cleaned screw-top Teflon beaker, dissolved in a combination of concentrated HF-HNO_3-HCl, and evaporated to dryness on a hot plate. The following procedures for the dried residue were the same as those described above for the fluid phase extracted from the run products.

Barium Concentration Analyses

As described above, a small fraction of each sample solution was diluted to ~1% HCl for Ba concentration analyses. The analyses were conducted using a Perkin-Elmer ELAN DCR-II inductively coupled plasma mass spectrometer (ICP-MS) at the CAS Key Laboratory of Crust-Mantle Materials and Environments, University of Science and Technology of China (USTC), Hefei. The procedures were described in Hou and Wang (2007). The relative standard deviation (RSD) of Ba concentration is better than 5 %.

Barium Isotope Analyses

Barium isotope analyses were performed at the CAS Key Laboratory of Crust-Mantle Materials and Environments, USTC, Hefei. All chemical procedures were carried out in an ISO-class 6 clean laboratory. The chemical purification of Ba was achieved by cation exchange chromatography with pre-cleaned resin (Bio-Rad 200-400 mesh AG50W-X12), following established procedures (Nan *et al.*, 2015, 2018). Sample solutions containing ~2 μg Ba were loaded onto the resin. The Ba recoveries through column chemistry, based on analyses of Ba concentration in the elution collected before and after the Ba cut, were >99%. The procedural blank was 2 ng Ba.

Barium isotope measurements were carried out on a Neptune Plus multi-collector inductively coupled plasma mass spectrometer (MC-ICP-MS), and a double-spike (^{135}Ba-^{136}Ba) technique was used to correct for instrumental mass bias. The "dry" plasma conditions (Aridus II desolvating nebuliser) were used to increase sensitivity. Barium isotope analyses were conducted in a low-resolution mode, with ^{134}Ba, ^{135}Ba, ^{136}Ba, ^{137}Ba and ^{138}Ba collected simultaneously by the L2, L1, C, H1 and H2 Faraday cups, respectively. ^{131}Xe and ^{140}Ce were also collected by the L4 and H3 Faraday cups to correct the effects of isobaric interferences from Xe and Ce. The background signals for ^{138}Ba (<0.03 V) were negligible relative to the sample signals (~30 V of the measured solutions with the Ba concentration of ~100 ppb).

The Ba isotopic data are reported in δ-notation in per mil relative to NIST SRM3104a, i.e., $\delta^{138/134}$Ba =

$[(^{138}Ba/^{134}Ba)_{sample}/(^{138}Ba/^{134}Ba)_{SRM3104a} - 1] \times 1000$. Based on replicate analyses of two in-house reference solutions USTC-Ba and ICPUS-Ba during this study, the external precision is better than 0.05‰ on $\delta^{138/134}$Ba (2SD). To monitor the accuracy, two reference materials G-2 and GSP-2 were processed through the column chemistry with samples. The $\delta^{138/134}$Ba values of granite G-2 (+0.01 ± 0.04 ‰, 2SD, *n* = 4) and granodiorite GSP-2 (-0.04 ± 0.05 ‰, 2SD, *n* = 6) obtained in this study agree well with previously published values within analytical uncertainties (+0.03 ± 0.04 ‰ and +0.04 ± 0.04 ‰ of G-2, and +0.02 ± 0.05‰ and 0 ± 0.04 ‰ of GSP-2; Nan *et al*., 2015, 2018; van Zuilen, 2016). For comparison, the published $\delta^{137/134}$Ba values have been converted to $\delta^{138/134}$Ba values by assuming mass-dependent fractionation following $\delta^{138/134}Ba \approx 1.33 \times \delta^{137/134}Ba$ (Horner *et al*., 2015).

Rayleigh Fractionation Model

The fraction of Ba in the residual melt (*f*) after fluid exsolution from melt can be defined as a function of the fraction of fluid exsolution (F) and $D_{FLUID\text{-}MELT}$ in Eq. S-1.

$$f = (1 - F)^{D_{FLUID-MELT}} \qquad \text{Eq. S-1}$$

The equilibrium Ba isotope fractionation factor (α) between fluid and melt is calculated based on the $\Delta^{138/134}Ba_{FLUID\text{-}MELT}$ described in Eq. 2.

$$\alpha \approx 1 + \frac{\triangle^{138/134}Ba_{FLUID-MELT}}{1000} \qquad \text{Eq. S-2}$$

With the *f* and α values calculated above, the Ba isotopic composition of the cumulative exsolved fluid and residual melt can be described by Eq. S-3 and Eq. S-4, respectively:

$$\delta^{138/134}Ba_{\text{exsolved } fluid} = \left(\delta^{138/134}Ba_{initial} + 1000\right)(f^{\alpha} - 1)/(f - 1) - 1000 \qquad \text{Eq. S-3}$$

$$\delta^{138/134}Ba_{residual\ melt} = (\delta^{138/134}Ba_{initial} + 1000)\, f^{(\alpha-1)} - 1000 \qquad \text{Eq. S-4}$$

where $\delta^{138/134}Ba_{initial}$ is the Ba isotopic composition of the initial fluid-saturated melt in nature. Supposing that the $\delta^{138/134}Ba_{initial}$ value equals to the average Ba isotopic composition of the upper continental crust (*i.e.* 0 ‰; Nan *et al*., 2018), the $\delta^{138/134}Ba_{\text{exsolved } fluid}$ and $\delta^{138/134}Ba_{\text{residual } melt}$ can be modeled using Eqs. 1, 2 and S-1 to S-4. Since the fluid content in silicate melts is usually less than 10 wt. % (*e.g*., Edmonds and Woods, 2018), up to 10 % fluid fraction (*i.e.* F = 0.1) is considered in the model.

Supplementary Figures

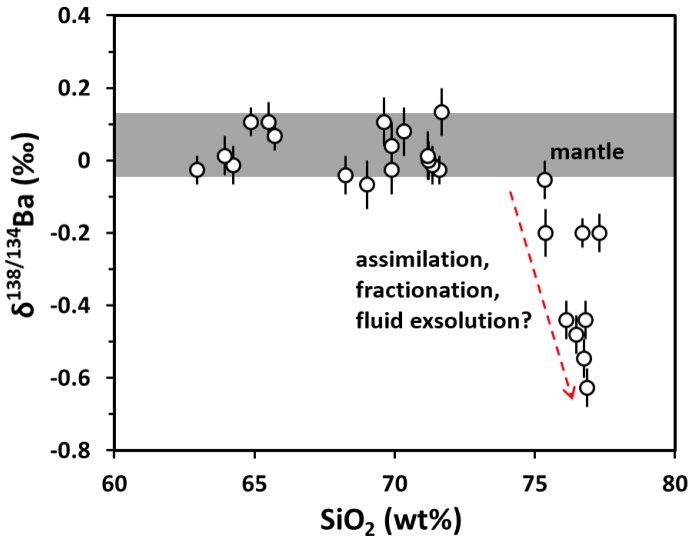

Figure S-1 $\delta^{138/134}$Ba vs. SiO_2 content of granite samples reported in Nan *et al.* (2018). Error bars represent 2SD uncertainties. The gray area represents the estimated average $\delta^{138/134}$Ba of the mantle (Li *et al.*, 2020). The $\delta^{137/134}$Ba reported in the literature has been converted to $\delta^{138/134}$Ba assuming mass-dependent fractionation following $\delta^{138/134}\text{Ba} \approx 1.33 \times \delta^{137/134}\text{Ba}$ (Horner *et al.*, 2015).

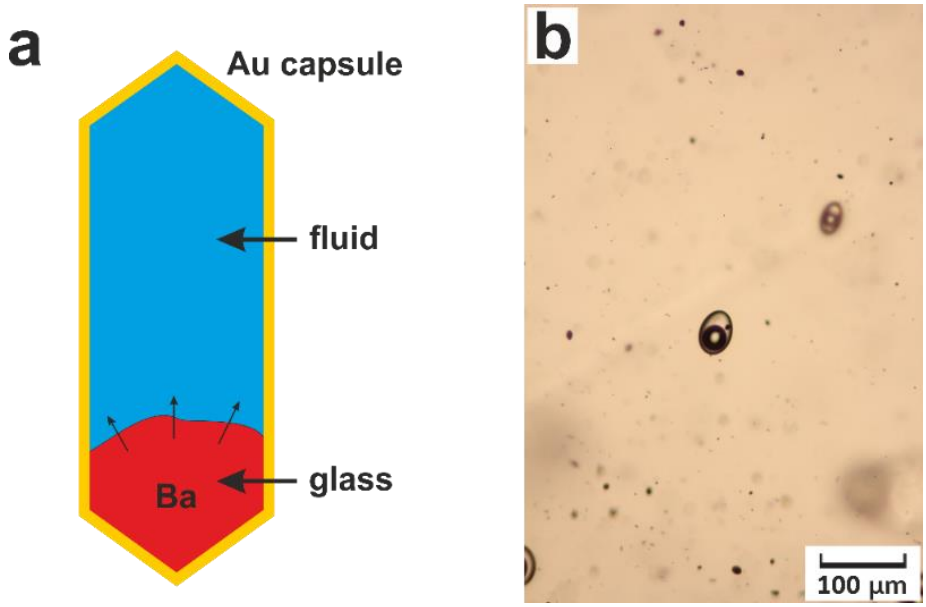

Figure S-2 (a) Experimental design with Ba-doped haplogranitic glass and (Na, K)Cl bearing fluid starting materials in a gold capsule. The outer diameter of the Au capsule is 4.3 mm. **(b)** A typical run product showing fluid inclusions in quenched glass (Run No. Ba05).

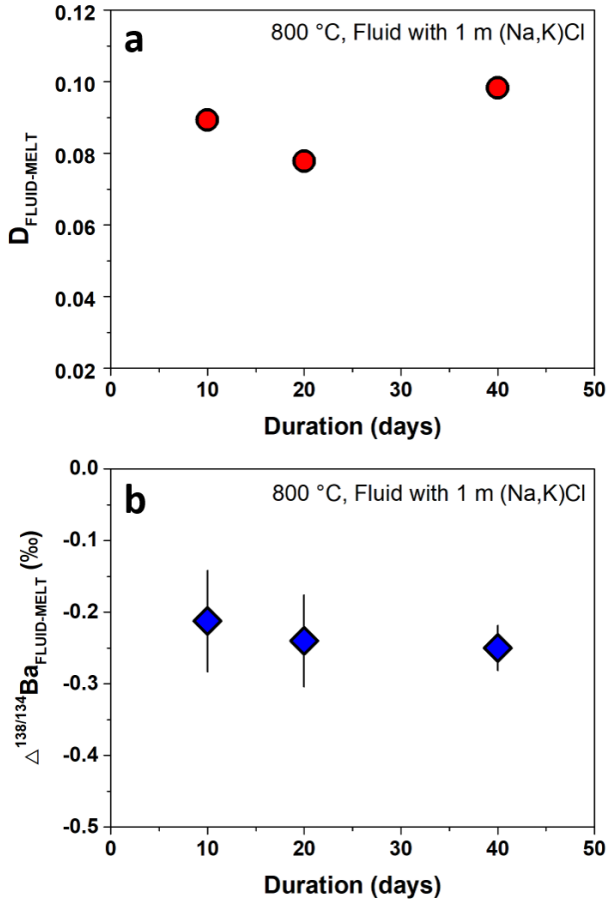

Figure S-3 Partitioning coefficient ($D_{FLUID-MELT}$) and isotope fractionation ($\Delta^{138/134}Ba_{FLUID-MELT}$) of Ba between aqueous fluid and silicate melt as a function of run durations (10, 20 and 40 days). Error bars in Figure S-3b represent 2SD uncertainties (see Table 1).

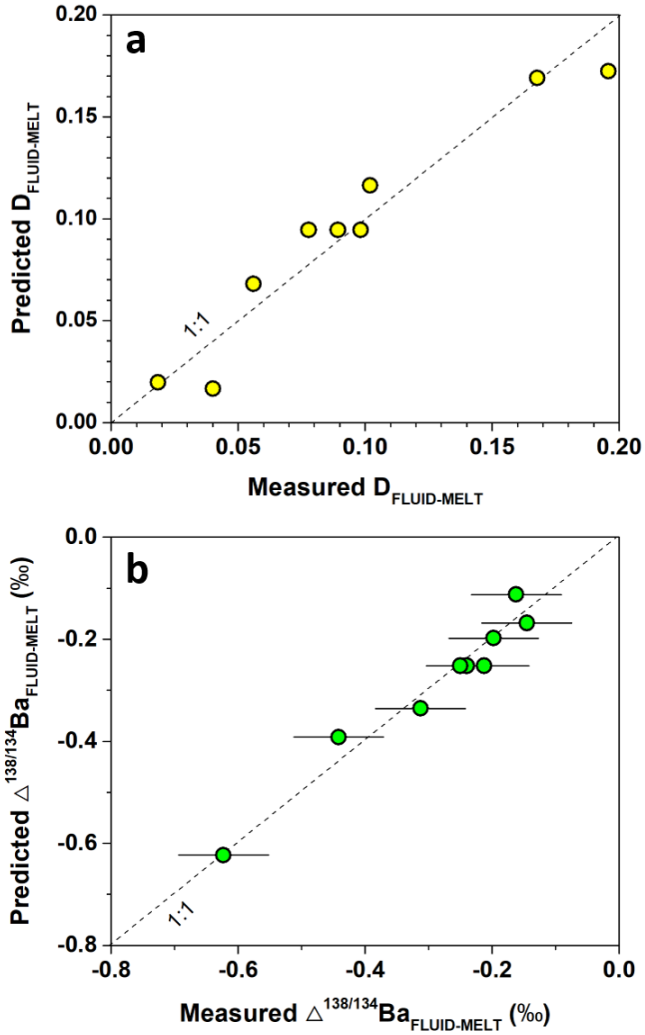

Figure S-4 Comparison between the experimentally measured data (Table 1) and predicted results based on Eqs. 1 and 2 for **(a)** partitioning coefficient of Ba ($D_{FLUID-MELT}$), and **(b)** equilibrium isotope fractionation of Ba ($\Delta^{138/134}Ba_{FLUID-MELT}$) between aqueous fluid and silicate melt.

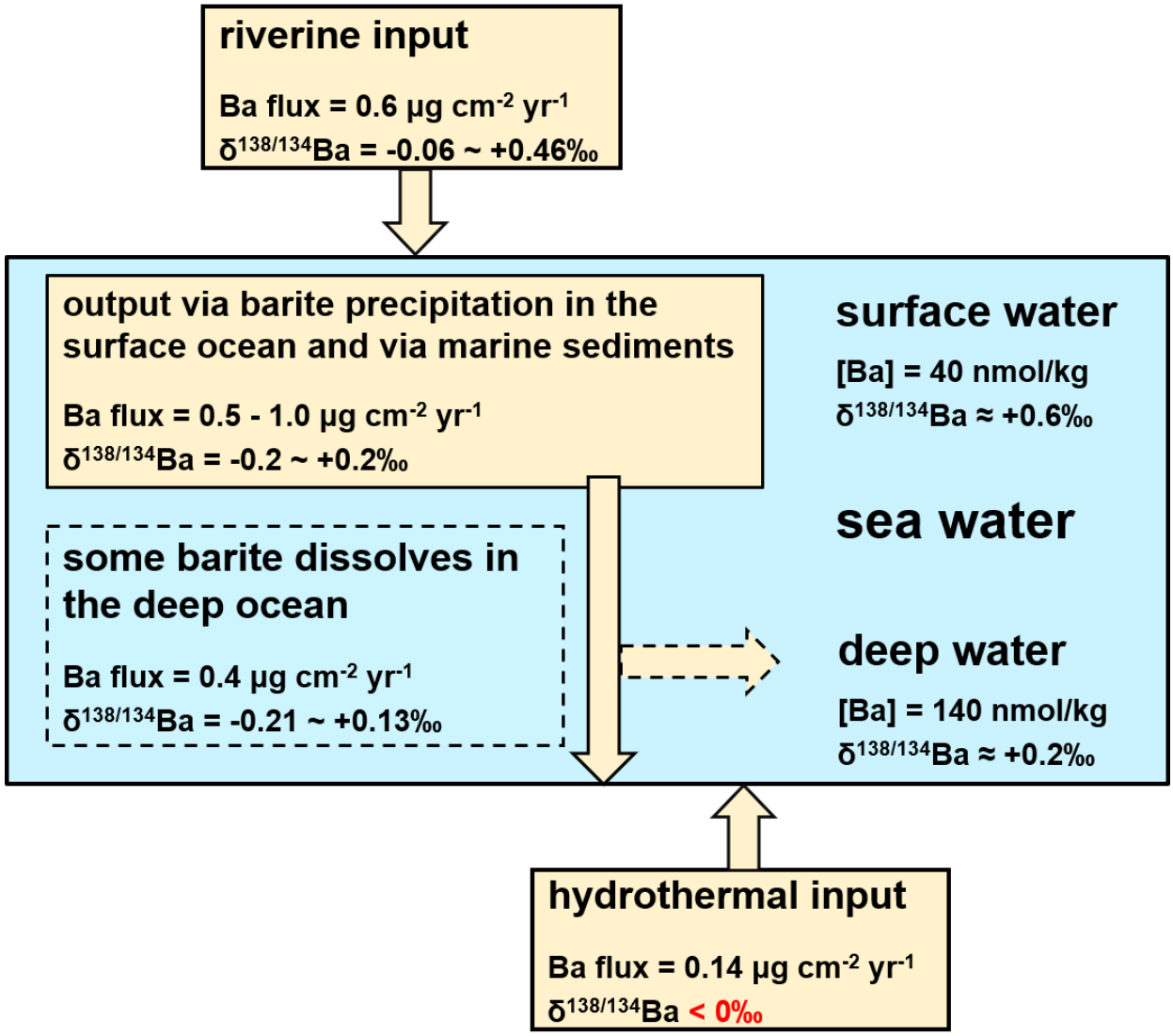

Figure S-5 A preliminary box model for the cycle of Ba and Ba isotopes in the ocean. Oceanic crust alteration is ignored in this model as the net alteration flux of Ba is insignificant (*e.g.*, Kelley *et al.*, 2003). The Ba fluxes of the riverine input, hydrothermal input, precipitation output, and barite dissolution, as well as the mean Ba concentrations of surface and deep sea water are from Dehairs *et al.* (1980) and Paytan and Kastner (1996). The $\delta^{138/134}$Ba of rivers are from Cao *et al.* (2016) and Gou *et al.* (2020). The $\delta^{138/134}$Ba of sea water are from Horner *et al.* (2015), Bates *et al.* (2017), Hsieh and Henderson (2017), and Bridgestock *et al.* (2018). The $\delta^{138/134}$Ba of barite and marine sediments are from Bridgestock *et al.* (2018, 2019), Nielsen *et al.* (2018), and Crockford *et al.* (2019).

Supplementary Information References

Bates, S.L., Hendry, K.R., Pryer, H.V., Kinsley, C.W., Pyle, K.M., Woodward, E.M.S., Horner, T.J. (2017) Barium isotopes reveal role of ocean circulation on barium cycling in the Atlantic. *Geochimica et Cosmochimica Acta* 204, 286-299.

Borchert, M., Wilke, M., Schmidt, C., Cauzid, J., Tucoulou, R. (2010) Partitioning of Ba, La, Yb and Y between haplogranitic melts and aqueous solutions: An experimental study. *Chemical Geology* 276, 225-240.

Bridgestock, L., Hsieh, Y.-T., Porcelli, D., Homoky, W.B., Bryan, A., Henderson G.M. (2018) Controls on the barium isotope compositions of marine sediments. *Earth and Planetary Science Letters* 481, 101-110.

Bridgestock, L., Hsieh, Y.-T., Porcelli, D., Henderson, G.M. (2019) Increased export production during recovery from the Paleocene–Eocene thermal maximum constrained by sedimentary Ba isotopes. *Earth and Planetary Science Letters* 510, 53-63.

Cao, Z., Siebert, C., Hathorne, E.C., Dai, M., Frank, M. (2016) Constraining the oceanic barium cycle with stable barium isotopes. *Earth and Planetary Science Letters* 434, 1-9.

Crockford, P.W., Wing, B.A., Paytan A., Hodgskiss, M.S.W., Mayfield, K.K., Hayles, J.A., Middleton, J.E., Ahm, A.-S.C., Johnston, D.T., Caxito, F., Uhlein, G., Halverson, G.P., Eickmann, B., Torres, M., Horner, T.J.. (2019) Barium-isotopic constraints on the origin of post-Marinoan barites. *Earth and Planetary Science Letters* 519, 234-244.

Dehairs, F., Chesselet, R., Jedwab, J. (1980) Discrete suspended particles of barite and the barium cycle in the open ocean. *Earth Planet. Sci. Lett.* 49, 528-550.

Edmonds, M., Woods, A.W. (2018) Exsolved volatiles in magma reservoirs. *Journal of Volcanology and Geothermal Research* 368, 13-30.

Gou, L.-F., Jin, Z., Galy, A., Gong, Y.-Z., Nan, X.-Y., Jin, C., Wang, X.-D., Bouchez, J., Cai, H.-M., Chen, J.-B., Yu, H.-M., Huang, F. (2020) Seasonal riverine barium isotopic variation in the middle Yellow River: Sources and fractionation. *Earth and Planetary Science Letters* 531, 115990.

Horner, T.J., Kinsley, C.W., Nielsen, S.G. (2015) Barium-isotopic fractionation in seawater mediated by barite cycling and oceanic circulation. *Earth and Planetary Science Letters* 430, 511-522.

Hou, Z., Wang, C. (2007) Determination of 35 trace elements in geological samples by inductively coupled plasma mass spectrometry. *Journal of University of Science and Technology of China* 37, 940-944.

Hsieh, Y.-T., Henderson, G.M. (2017) Barium stable isotopes in the global ocean: Tracer of Ba inputs and utilization. *Earth and Planetary Science Letters* 473, 269-278.

Johannes, W., Holtz, F. (1996) Petrogenesis and Experimental Petrology of Granitic Rocks, Springer, Berlin, 335 p.

Kelley, K.A., Plank, T., Ludden, J., Staudigel, H. (2003) Composition of altered oceanic crust as ODP Sites 801 and 1149. *Geochemistry Geophysics Geosystems* 4, 8910.

Keppler, H. (2010) The distribution of sulfur between haplogranitic melts and aqueous fluids. *Geochimica et Cosmochimica Acta* 74, 645-660.

Keppler, H. (2017), Fluids and trace element transport in subduction zones, *American Mineralogist* 102, 5-20.

Keppler, H., Wyllie, P.J. (1991) Partitioning of Cu, Sn, Mo, W, U, and Th between melt and aqueous fluid in the systems haplogranite-H_2O-HCl and haplogranite-H_2O-HF. *Contributions to Mineralogy and Petrology* 109, 139-150.

Li, W.-Y., Yu, H.-M., Xu, J., Halama, R., Bell, K., Nan, X.-Y., Huang, F. (2020) Barium isotopic composition of the mantle: Constraints from carbonatites. *Geochimica et Cosmochimica Acta* 278, 235-243.

Matthews, W., Linnen, R.L., Guo, Q. (2003) A filler-rod technique for controlling redox conditions in cold-seal pressure vessels. *American Mineralogist* 88, 701-707.

Nan, X., Wu, F., Zhang, Z., Hou, Z., Huang, F., Yu, H. (2015) High-precision barium isotope measurements by MC-ICP-MS. *Journal of Analytical Atomic Spectrometry* 30, 2307-2315.

Nan, X.-Y., Yu, H.-M., Rudnick, R.L., Gaschnig, R.M., Xu, J., Li, W.-Y., Zhang, Q., Jin, Z.-D., Li, X.-H., Huang, F. (2018) Barium isotopic composition of the upper continental crust. *Geochimica et Cosmochimica Acta* 233, 33-49.

Paytan, A., Kastner, M. (1996) Benthic Ba fluxes in the central Equatorial Pacific, implications for the oceanic Ba cycle. *Earth and Planetary Science Letters* 142, 439-450.

van Zuilen, K., Nägler, T.F., Bullen, T.D. (2016) Barium isotopic compositions of geological reference materials. *Geostandards and Geoanalytical Research* 40, 543-558.

Wallace, P.J. (2005) Volatiles in subduction zone magmas: concentrations and fluxes based on melt inclusion and volcanic gas data. *Journal of Volcanology and Geothermal Research* 140, 217-240.